University of Sheffield | School of Mechanical, Aerospace & Civil Engineering

BEng Mechanical Engineering

Effect of Geometry on Apparent Stiffness of Triply Periodic Minimal Surface Porous Scaffolds for Orthopaedics Implants

Zhe Wei KHO

May 2025

Vee San CHEONG

Thesis submitted to the University of Sheffield in partial fulfilment of the requirements for the degree of Bachelor of Engineering

Word count: 4698

ABSTRACT

Orthopaedic implant longevity remains a critical challenge, particularly for younger and more active patients, due to complications such as aseptic loosening and stress shielding. The decline in performance of cemented implants has prompted a shift toward cementless fixation methods, where osseointegration is facilitated through porous scaffold geometries. Among various configurations, sheet-type Triply Periodic Minimal Surfaces (TPMS) have gained attention for their structural efficiency, mechanical performance, and superior bone ingrowth characteristics.

This study aimed to develop and optimise gyroid, diamond, and Schwarz primitive sheet-TPMS scaffolds to match the apparent stiffness of trabecular bone (~3 GPa), enabling better biomechanical compatibility in orthopaedic applications. A novel computational workflow was implemented using Python automation integrated with nTop and ANSYS Mechanical to generate and iteratively simulate scaffold geometries.

An automated optimisation routine based on the secant method enabled convergence to target stiffness values with less than 5% deviation within six iterations per geometry type. Validation against the Gibson-Ashby model showed strong agreement for gyroid and diamond types, although higher deviations were observed for the primitive geometry, highlighting sensitivity to unit cell configuration.

Results confirmed that apparent stiffness scales with the thickness-to-cell-size ratio and revealed significant stiffness changes when transitioning from single to multi-cell configurations. While the numerical approach proved efficient and accurate, practical limitations such as manufacturing constraints at low thicknesses and unaccounted effects of partial bone ingrowth pose challenges for clinical translation.

Overall, this study demonstrates a scalable and precise method for designing stiffness-matched TPMS scaffolds, with future work suggested in extending optimisation frameworks to include manufacturing variability and long-term biological integration factors.

CONTENTS

ACKNOWLEDGEMENTS

It's remarkable that it has already been three years since the start of this degree. At the same time, I feel somehow the months have just slipped by. Regardless, I'm glad to have grown so much over the past few years.

I would not have been able to reach this point without the guidance of my supervisor, Vee, who provided the initial idea for this project. It pains me that I have not been able to perform at my best. However, I'm truly grateful for the countless hours of conversations we've had together. It's been an honour working with you.

In addition, I would like to mention special thanks to everyone I have met at Project Hex (and Avis Drone Labs). They have been absolutely inspirational in my engineering journey thus far and have fundamentally transformed my perspective on what I thought I was capable of. While we didn't achieve our goals, the spirit of pushing ourselves to achieve our best, is something I will never forget.

I would also like to mention my academic tutor, Marco, for being a dear friend and mentor for me over the last few years. My course mates – Shreyas, Cheng, Jason, Lukas, Anson, Sarwin and Musaib for making the late study nights fun. Matius as well, for always being there when I needed it the most.

Last, but not least. I would like to dedicate this project to my parents for their support over the last three years. I wouldn't be able to be here without them.

1 BACKGROUND

1.1 Introduction

Total hip and knee replacement (THR and TKR) are one of the most common operations conducted when treating arthritis [1] [2] [Learmonth] [nice]. In the United Kingdom (UK), these procedures account for approximately £2 billion of the National Health Service (NHS) budget [nice]. With THR and TKR procedures projected to increase by almost 40 percent by 2060, it is critical that improvements are made in the area to better serve the growing demographic [3] [4].

Recent meta-analyses on joint registry data have identified a concerning issue with the design of implants. Reports have found that in the UK, only 58% of THRs last up to 25 years, with TKRs fairing at 82% success rate [1] [2]. On average, this translates to *three in every ten patients facing* complications down the line after undergoing a replacement procedure. In addition, younger patients risk having to undergo constant revision surgeries from implant failure. Individuals aged 50 to 59 years old have a *three to five times greater long-term risk of revision* than those aged 70 to 79 [5].

Studies are suggesting that the use of bone cement as a fixation method is the main reason to the decrease in implant longevity [6]. Despite the established use of cemented implants as the gold standard in joint replacements since the 20th century [7], the capacity for local antibiotic delivery while effective only prevents early postoperative bacterial infections and is less beneficial to the patient in the long term. The decline in the quality of the bone-cement interface over time eventually leads to premature loosening as seen in Figure 1.1 [6] [8]. As a result, studies are warning against the use of cemented implants for younger, more active and obese patients [8] [9].

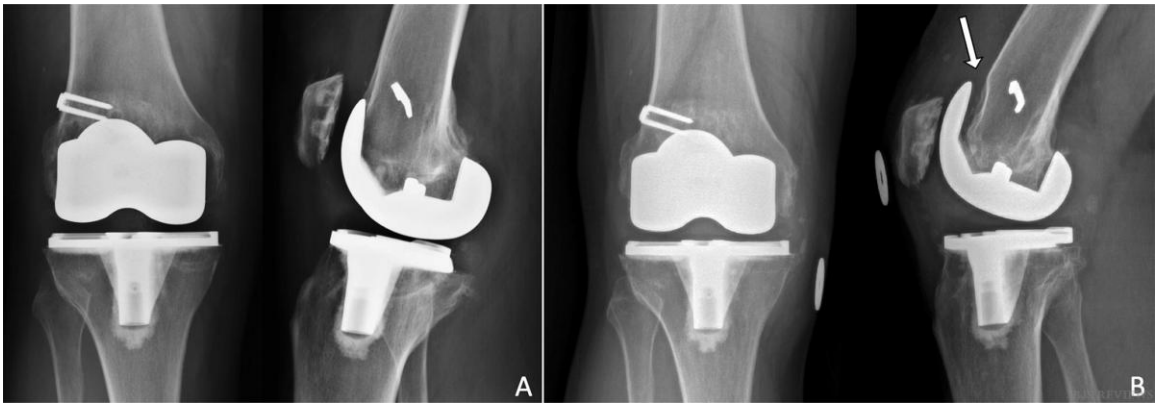

Figure 1.1. Comparison of a TKA operation using a cemented implant, immediately post-operation (left), and five years after (right) where aseptic loosening can be seen. Adapted from **[8]**.

In contrast, cementless fixation is becoming an increasingly reliable approach with minimal intervention required post-operation in the long term. Success rates upwards of 95 percent after ten years have been reported in literature for cementless fixation, [7] [8] [9] [10]. A key interaction that governs successful fixation in this method is the integration of bone with the implant, as shown in Figure 1.2 [11]. With this, compressive, tensile, and shear loads can therefore be shared between the two bodies, smoothening the transition between two dissimilar materials [12].

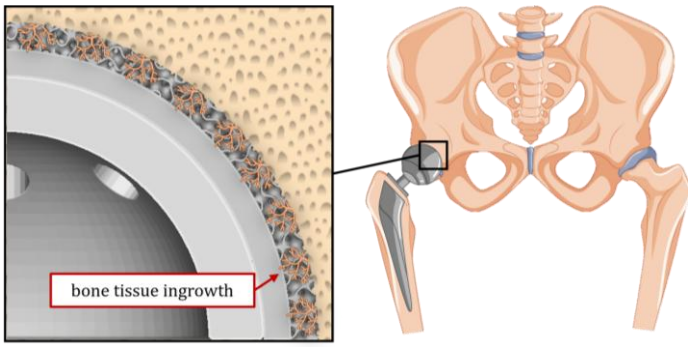

Figure 1.2. An acetabular cup for THR which uses cementless fixation. Porosity allows bone tissue to grow into the implant surface, also known as osseointegration or bone ingrowth.

As pictured in Figure 1.3, there are multiple methods of creating porosity within cementless implants. Common 'traditional' processes used by manufacturers include sintering metal beads onto the implant surface or plasma spraying to achieve a roughened finish [8] [10, pp. 253-255]. Popularised during the first generation of cementless implants between 1970 and 1980, implants such as the Kodama-Yamamoto Mark-I model often used these methods to achieve bonding [13]. However, in recent years, new findings have uncovered that stiffness of the porous surface is essential towards achieving optimal bone ingrowth and longevity [14]. This has resulted in additive manufacturing (AM) garnering significant attention due to the design flexibility it offers. Known as *metamaterials* or *porous scaffolds*, significant potential remains in improving patient outcomes in the long term [12] [15].

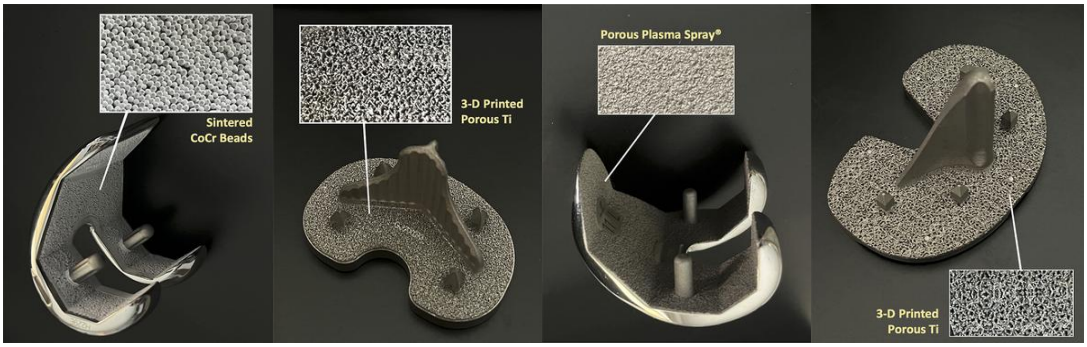

Figure 1.3. Examples of porous surfaces used in implants for TKR from major manufacturers, Stryker and Zimmer-Biomet. Adapted from **[8]**.

1.2 Porous Scaffolds: Geometry and Bone Ingrowth

Porous scaffolds at the primitive level are structures which contain small voids. Examples of them exist all around us and can be organised into two categories, namely stochastic and cellular designs.

Stochastic designs attempt to replicate the inherent imperfections that exist in everyday life. In the context of bone tissue, some researchers have explored recreating the irregular structure that resembles it (specifically trabeculae) [16]. Conversely, cellular configurations utilise a single unit cell that is periodically repeated, as seen in Figure 1.4. These can be strut-based designs which contain beams that are arranged in geometric patterns; or triply periodic minimal surfaces (TPMS) which are infinite surfaces and locally minimise surface area for a given boundary [17] [18] [19].

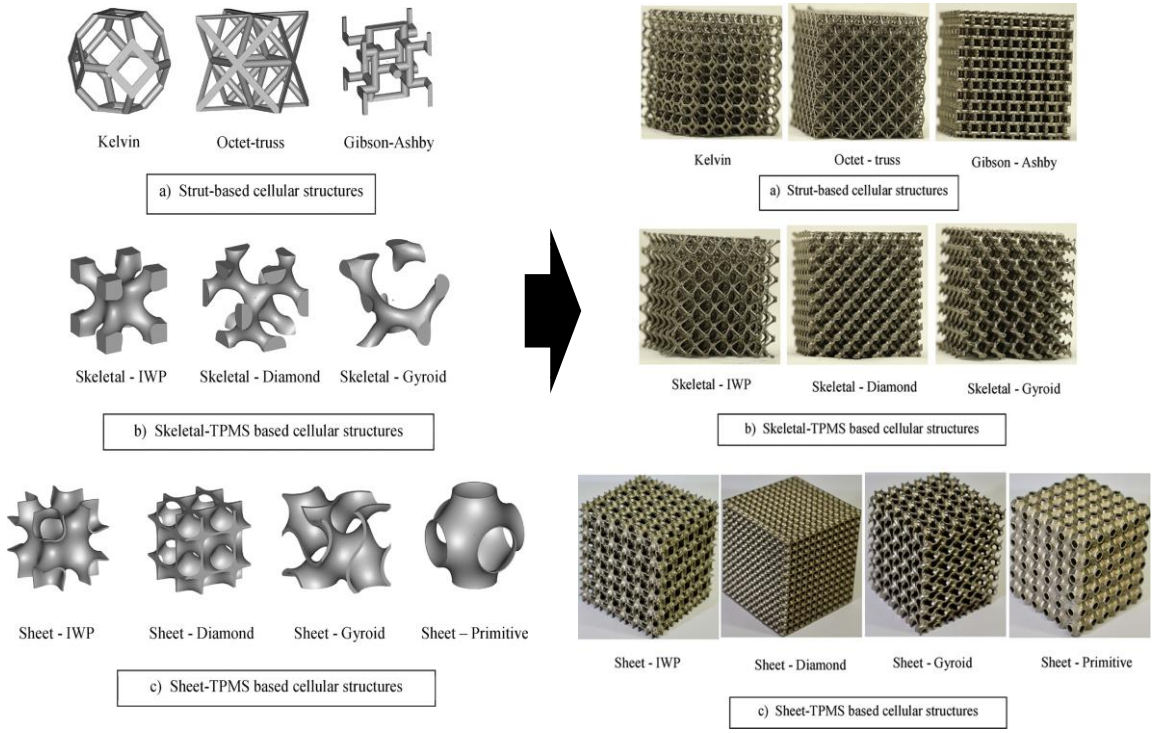

Figure 1.4. Strut-based, skeletal-TPMS and sheet-TPMS as unit cells (left), then periodically repeated and manufactured using selective laser melting (right). Adapted from **[17]**.

Comparing the three types of scaffolds and the requirements under the lens, several features stand out for TPMS geometries, particularly the sheet-TPMS configuration. First, the zero net curvature of sheet-TPMS geometry has been theorised and experimentally proven to be most effective for bone adhesion and proliferation due to the preference for tissue growth on concave surfaces [15] [20]. The sheet-TPMS architecture also generally has higher pore interconnectivity which allows improved permeability and thus allows sufficient nutrition and oxygenation of bone tissue cells [18]. Furthermore, stress concentrations are also minimal due to their smooth contours which reduces the chance

for fatigue failure in the long run [20]. Combined with higher structural stiffness and strength over other geometries [17] [18] [20], sheet-TPMS geometries ultimately lead to minimal material usage for manufacturers and subsequently lower costs for consumers. Altogether, the benefits of sheet-TPMS geometries show potential in becoming the ideal geometry for biomedical implants.

While geometry is important, the size of the voids within porous scaffolds is also significant and has seen significant discussion within the scientific community. Research from Taniguchi et al showed that measuring the diameter of the voids (pore size) could influence tissue growth rates over time. They identified that a pore size around 600 micrometers would be most effective [21]. A similar observation was seen in a study by Cheong et al, where 700 micrometers proved to better compared to an implant with a pore size of 1500 micrometers [22]. However, in a review conducted by Karageorgiou and Kaplan, their findings recommended pore sizes to be greater than 300 micrometers instead [23]. Other studies have also shared mixed responses, suggesting pore sizes that range from as low as 150 micrometers [24], to 490 micrometers [25], up to 710 micrometers [26].

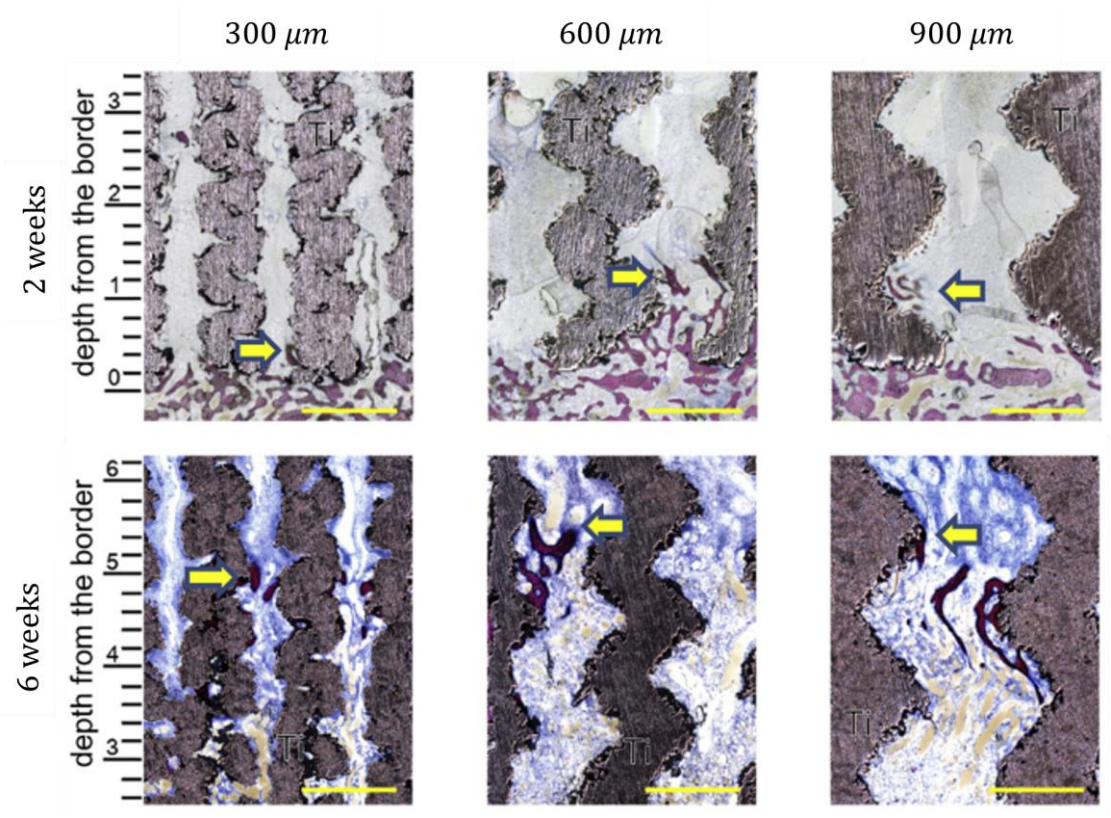

Figure 1.5. Cross section of porous scaffolds after in vivo experiment showing bone ingrowth at 2 weeks and 6 weeks. Effectiveness in the near term was investigated for scaffolds with pore sizes of 300, 600 and 900 micrometres. Adapted from [Taniguchi].

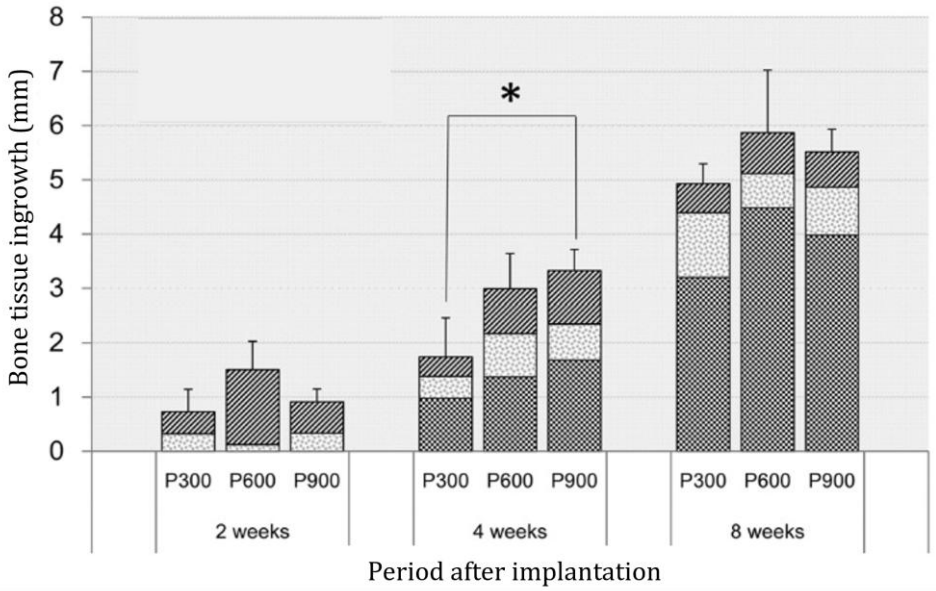

Figure 1.6. Chart showing summary of the results from the in vivo experiment conducted by Taniguchi et al. Porous scaffold with pore size of 600 micrometres had the highest bone ingrowth throughout the whole period, except at 4 weeks. Adapted from [Taniguchi]

Porosity is measured by calculating the volume of space in the overall volume occupied. Interestingly, in contrast to pore size, only minimal differences have been observed when porosity serves as the independent variable. Van der Stok et al showed that changing porosity from 60 percent to 80 percent does not significantly impact bone ingrowth [25]. However, this observation is not in line with the fact that altering porosity does impact implant integrity down the line, as discussed in Section 1.3.

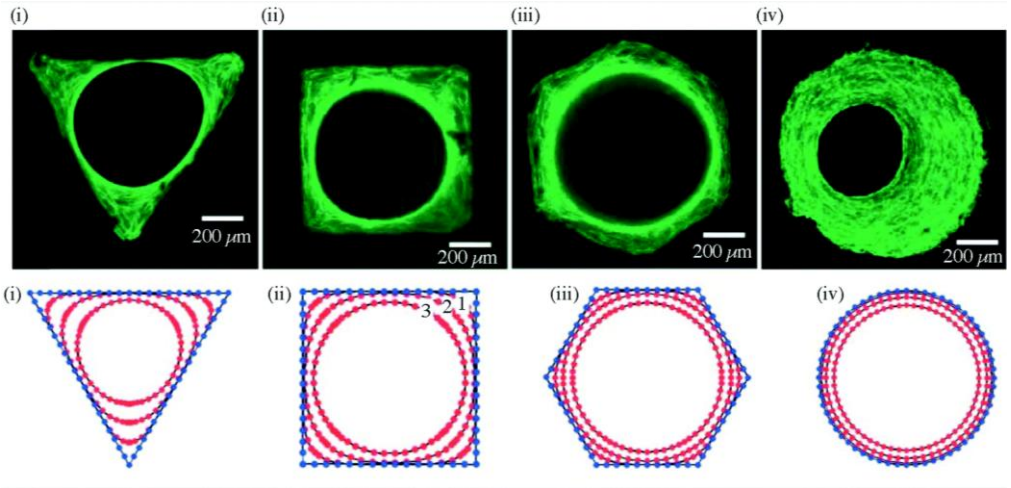

Figure 1.7. Tissue growth on various surface geometries of the same material. From left to right: triangular, rectangular, hexagonal, and concave/circular. Tissue growth is most significant on concave/circular surfaces. Adapted from **[15]**

1.3 Porous Scaffolds: Materials, Mechanical Properties and Longevity

Designing porous scaffolds requires careful consideration of implant and the surrounding bone tissue. This starts with considering the materials.

Metal alloys have often been used in orthopaedic implants due to their biocompatibility and strength. These properties are essential towards ensuring patient outcomes. For instance, titanium (Ti) alloys offer low elastic modulus, high biocompatibility, excellent additive manufacturing properties, and high strength to density ratio [27]. Ti-6Al-4V at an elastic modulus of 110 GPa remains a strong candidate and is currently used in most commercially available implants [22] [28].

In contrast, the elastic modulus of trabecular bone is significant lower with a range around 0.5 GPa to 22.5 GPa, with significant variation as shown in Figure 1.8. In addition, trabecular bone stiffness varies depending on age, patient health conditions and demographics [29]. This is consistent with the observations made by researchers when installing implants for younger patients, as mentioned in Section 1.1.

This mismatch in stiffnesses results in implant loosening from bone resorption, also known as stress shielding (breaking down of bone tissue due to lack of exertion over time) [22]. Tailoring the stiffness of bone implants to trabecular bone for each patient must be done to achieve better long-term outcomes. Porous scaffolds assist in this area by lowering the stiffness to a similar value to trabecular bone tissue.

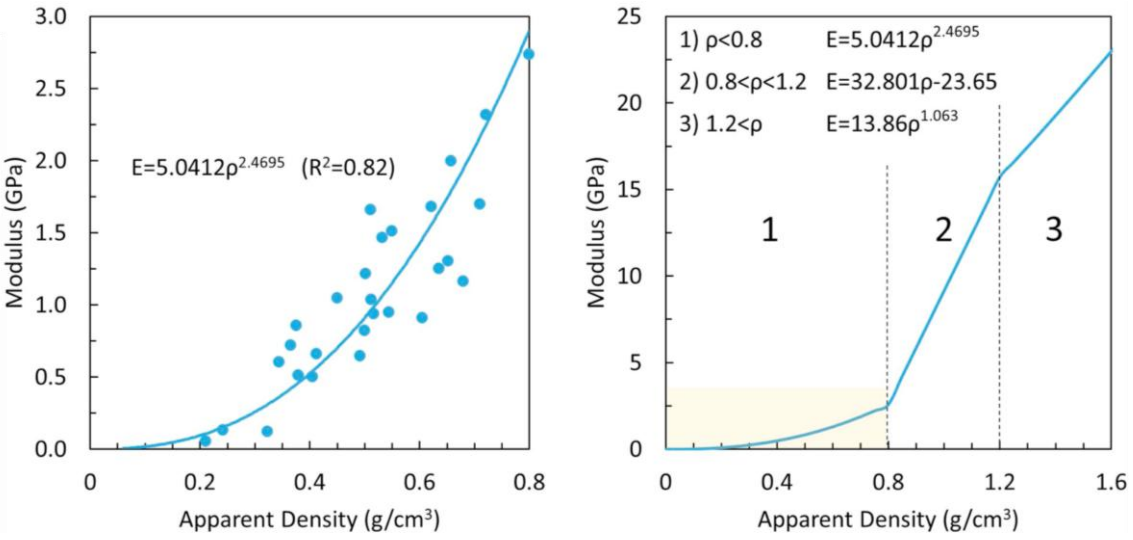

Figure 1.8. Elastic modulus of trabecular bone tissue against apparent density (measured mass over volume occupied) under quasi-static compression. Left shows the range from 0 to 0.8 g/cm^3 and right shows the range from 0 to 1.6 g/cm^3 (right). Adapted from **[16]**.

Increasing the porosity of a scaffold generally reduces the overall elastic modulus (apparent stiffness) as the deformation experienced by the scaffold increases. However, when designing scaffolds for optimum long-term performance, high fatigue strength is also a key criterion [8] [30]. Engineering scaffolds that meet both characteristics at the meso-scale is highly important.

With regards to sheet-TPMS designs, it excels in both departments. As seen in Figure 1.9, where sheet-TPMS designs held the highest yield strength values at the same porosity of material. Consequently, Bobbert et al showed that sheet-TPMS have three times higher fatigue yield strength compared to strut-based designs. In their study, scaffolds with porosity between 50 to 70 percent were subject to 1,000,000 ($1x10^6$) load cycles at 60 percent yield strength with successful effect. This was higher than the 20 percent yield strength which strut-based designs were capable of in literature [18].

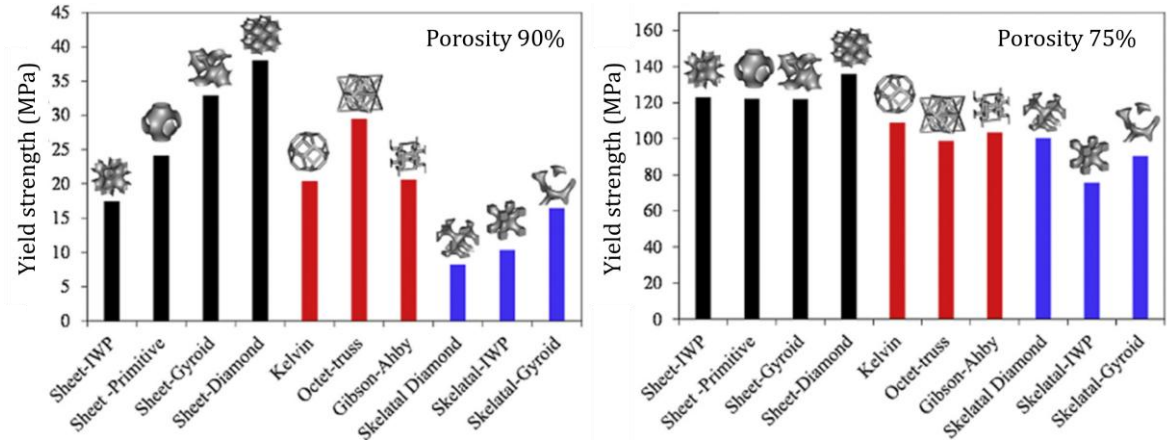

Figure 1.9. Comparison of the yield strength (MPa) of porous scaffolds at a porosity of 90 percent (left) and 75 percent (right). Sheet-TPMS designs at both porosities outperform other configurations. Adapted from **[17]**

Multiple studies have also demonstrated the importance of considering the transient nature of bone growth. For instance, the mechanical properties of scaffolds have been shown to increase by a factor of 2-7 when bone grows into a scaffold [14]. This behavimy can be likened to the behavimy of a composite, where bone acts as a matrix, whereas the scaffold acts as a fibre. Retrospectively, partial bone ingrowth strengthens the scaffold and changes the stress concentrations within the scaffold, causing scaffolds with stress concentrations to become susceptible to failure [22]. Therefore, optimising an implant to the desired mechanical environment immediately post-surgery alone may not be sufficient to sustain long-term bone ingrowth [19] [22] [28].

1.4 Porous Scaffolds: Optimisation Methodologies

Porous scaffolds, especially sheet-TPMS structures, require drastically different optimisation strategies. Unlike most geometries, as of writing, no analytical solutions exist for these complex structures, as such manual (trial-and-error) and experimental (design of experiment, interpolation) methods are often used to achieve optimisation, as seen in Table 1. This is related to the challenges associated with modelling and analysing these geometries.

Table 1. Modelling and optimisation methods used for porous scaffolds.

Type	Modelling Strategy	Optimisation	Ref.
Stochastic	Implicit modelling of line geometry in Rhino 5.0 (Robert McNeel & Associates, USA) direct to manufacturing.	Gibson-Ashby Interpolation	[16]
TPMS	Implicit modelling of surface and exported as STL via MATLAB (Mathworks Inc, USA).	Gibson-Ashby Interpolation	[31]
TPMS	Implicit modelling of surface via K3Dsurf; OBJ to STL via MeshLab; thicken in ABAQUS/CAE 6.13; final design in Magics (Materialise NV, Belgium).	Manual	[18]
TPMS	Implicit modelling of body and exported as STL in nTop (nTopology Inc, USA).	Manual	[32]
TPMS	Implicit modelling of body and exported as STL in custom open-source Python application.	N/A*	[33]
TPMS	Implicit modelling of surface via Rhino 6.0 (Robert McNeel & Associates, USA) with Grasshopper plug-in; final design in Magics (Materialise NV, Belgium).	N/A*	[34]
TPMS	Implicit modelling of surface and exported as STL via MATLAB (Mathworks Inc, USA).	N/A*	[35]

* = method of optimisation not explicitly mentioned

Sheet-TPMS scaffolds are challenging to model because of their complex curvatures. Geometries in current computer aided design (CAD) software packages such as Siemens NX, Catia, Creo, SOLIDWORKS, and Fusion 360 are modelled as boundary representations (b-reps). B-reps use a collection of 2D faces in a 3D plane and connected to form a volume by defining shared edges and vertices between faces, as seen in Figure 1.10 [36].

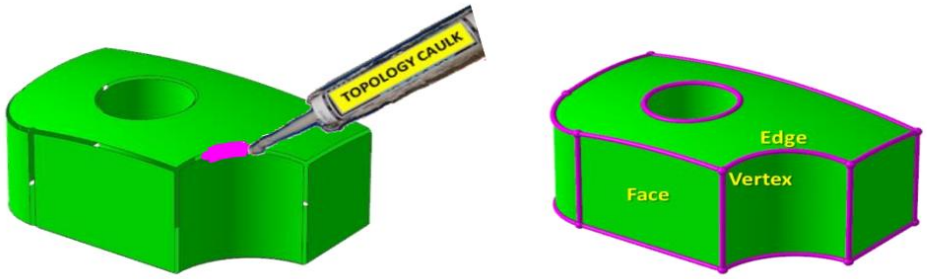

Figure 1.10. B-rep modelling is similar to gluing the edges of pieces of cardboard together to form a box. Adapted from **[36]**

The number of faces necessary to apply sheet-TPMS scaffolds to real-life applications is extremely high when modelling in the b-rep environment, making it computationally inefficient to work with.

The solution to this has been implicit modelling which is capable of effectively modelling porous scaffolds accurately without high resource consumption. Unlike b-reps, objects are significantly simpler as they are defined using mathematical functions in the form of scalar fields. In essence, this allows up to around 30-60 times reduction in file size and modelling complex, optimised designs without sacrificing significant memory [36]. In addition, geometry accuracy can be guaranteed with implicit modelling regardless of the complexity of the problem presented [35].

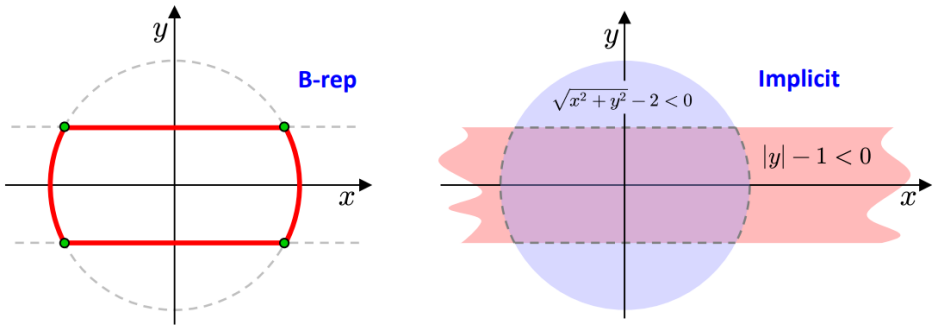

Figure 1.11. A comparison between b-rep and implicit methods when modelling 2D geometries. Reprinted from [Allen].

As a result, this has seen startup software, nTop (nTopology Inc, USA), a pioneer in the space, become an increasingly popular option for modelling systems and components for additive manufacturing. Its direct integration with manufacturing, substantial support for cellular structures (Figure 1.12), and native support for automation are several of its standout features. More recently, Siemens Energy has adopted this modelling strategy to support their additive manufacturing capabilities for developing advanced heat exchangers [37].

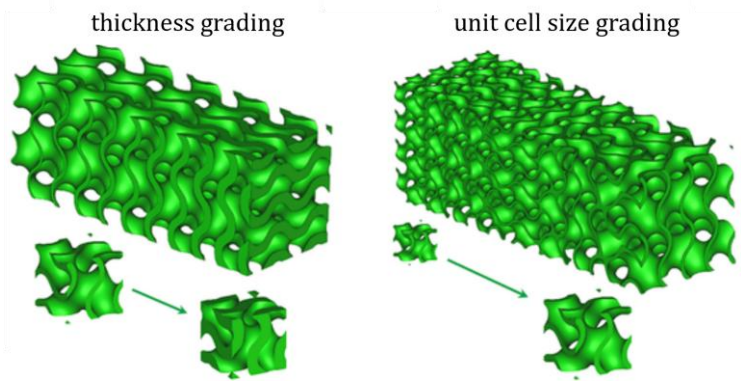

Figure 1.12. Functional grading of cellular structures such as thickness and unit cell size, a feature of nTop (nTopology Inc, USA). Adapted from [Al-Ketan Functionally Graded].

When designing scaffolds to match the stiffness of trabecular bone, most studies rely on experimental approaches [16] [18] [21]. These typically use design of experiments (DOE) methodologies, followed by interpolation of results to achieve the desired stiffness values. While this approach is reliable, it is often time-consuming and costly, as it requires a large number of samples to build a robust dataset for analysis. For example, Bobbert et al. conducted research involving 96 samples to characterize the static properties of four types of sheet-TPMS scaffolds across four porosities [18].

Given the potential emergence of new scaffold geometries in the future, it is crucial to efficiently understand their properties through computational methods. Therefore, advancing computational techniques is essential to drive progress in this field.

1.5 Aims and Objectives

In summary, the implementation of sheet-TPMS scaffolds for orthopaedic implants holds significant potential. While understanding of these designs is well developed, optimisation of scaffolds has not seen much attention despite the importance for matching the apparent stiffness to the elastic modulus of trabecular bone tissue. This is due to the resource consuming process involved to achieve optimisation.

This study aims to understand how geometry informs the mechanical properties of additively manufactured sheet-TPMS porous scaffolds, when matched to the desired apparent stiffness. The main areas of focus are to:

1. Establish a method capable of designing optimised TPMS porous scaffolds within four hours with a convergence criterion of less than 5 percent deviation from the desired stiffness.
2. Design three types of sheet-TPMS porous scaffolds (gyroid, diamond, Schwarz primitive) that are optimised to a stiffness of 3 GPa.
3. Investigate the mechanical performance of the TPMS porous scaffolds under static loading conditions when changing parameters.

2 METHODOLOGY

2.1 Overview

To achieve the project's objectives and ensure repeatable results, a Python-based optimization script was developed to tailor porous scaffolds to the desired stiffness values (Appendix A). Python was selected for its seamless integration with the simulation APIs used in scaffold testing. This involved three steps:

- **Meshing and Modelling**: Developing the scaffold geometry and optimal meshing parameters.
- **Verification & Validation**: Confirming numerical accuracy of model with existing data.
- **Sensitivity Analysis**: Investigating various boundary conditions and geometry.

Initial studies were first done on a single scaffold type – the gyroid (G). This guided the selection of the **initial** input parameters and ensured that the right element size was chosen. Once the model was verified and validated, the script was expanded to other types of geometries.

Despite the many options, Gyroid (G), diamond (D) and Schwarz primitive (P) sheet-TPMS geometries were the only three geometries chosen due to the large amount of literature data available on them. These were modelled using the equations shown in Appendix B, and preliminary data was obtained for validating the optimised designs, as discussed in Section 2.4.

Due to limits in computational power, analysis was mostly carried out using a single unit cell. The final framework developed is presented in Figure 2.1.

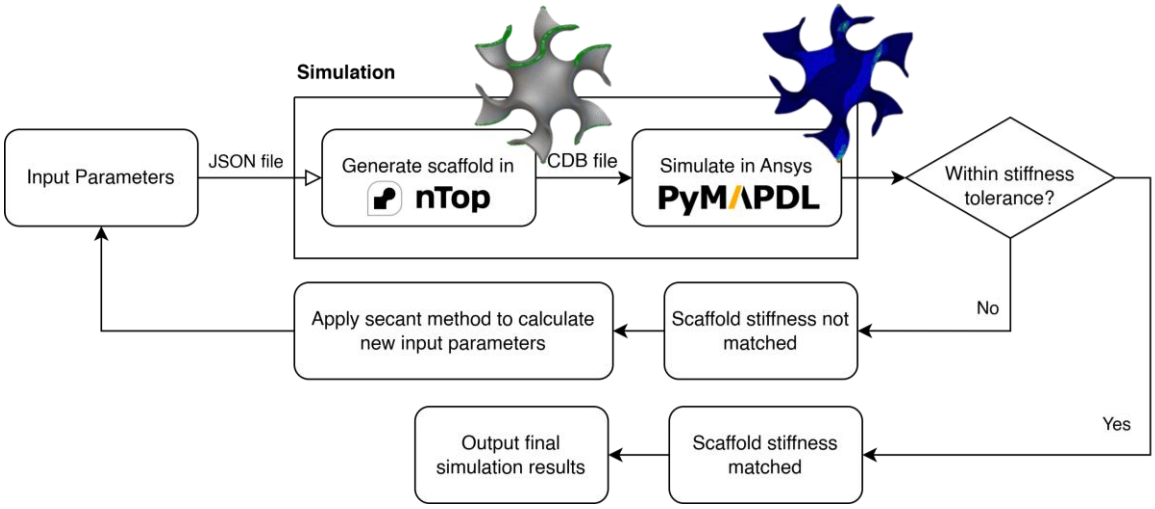

Figure 2.1. Flowchart for optimising scaffolds to desired stiffnesses accurately showing how decisions were made.

2.2 *Simulation: Meshing and Modelling*

The framework operates by first generating the geometry in nTop Automate 5.16.2 (nTopology Inc, USA) by leveraging nTop's built-in cellular structure library.

Input parameters were loaded as a JSON file which specifies the *TPMS type, cell size, TPMS thickness, and element size*. An example of how each sheet-TPMS scaffold was defined in nTop is shown in Figure 2.2.

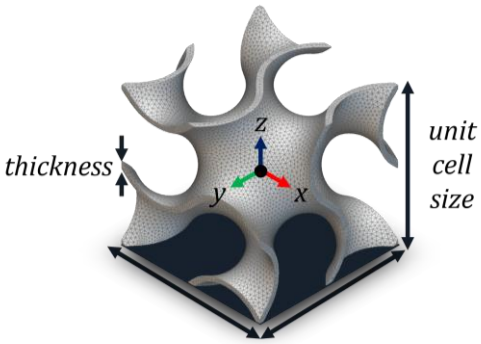

Figure 2.2. A gyroid sheet-TPMS scaffold as defined in nTop, which requires the thickness and unit cell size. In nTop, scaffolds exist as cells, which are periodically repeated to create different configurations.

Once the geometry was implicitly modelled, the geometry was processed through a meshing routine outlined in Figure 2.3.

Remeshing the surface geometry was required to control the mesh so that the desired element size could be achieved. In addition, small or floating geometrical features were deleted to avoid unconstrained errors in finite element analysis (FEA). Finally, named selections for boundary conditions were created by boolean selection before exporting the geometry as a CDB file.

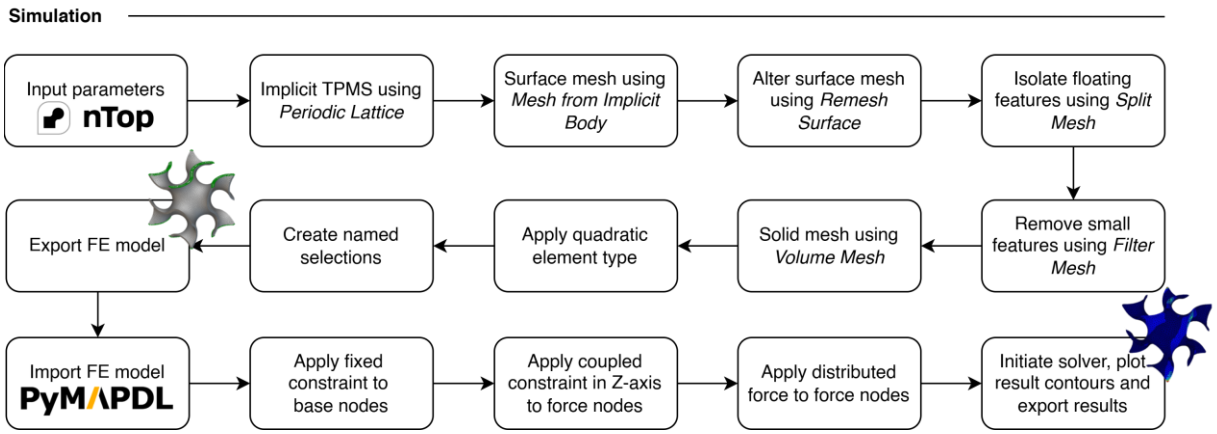

Figure 2.3. Flowchart showing the modelling, meshing and finite element analysis workflow. Words in italics refer to the function used in nTop.

After setting up ANSYS Mechanical APDL 2024 R2 (ANSYS Inc, USA) using PyMAPDL 0.68.2, the CDB file was imported. Material properties of Ti-6Al-4V were then defined with an elastic modulus of 110 GPa, Poisson's ratio of 0.34 and density of 4510 kg/m^3.

The element type used was 10-node tetrahedrals (Tet10), also known as SOLID187. This allowed the results in the mesh to converge much more efficiently than linear elements, with improved accuracy.

As shown in Figure 2.4, the top surface was not constrained to reflect the environment scaffolds experience on the surface of an implant.

- **Force nodes**: force of -100 N was chosen as only stiffness is of concern in this study. Kinematic constraints were applied in the z-axis.
- **Base nodes**: fixed constraint simulated how the base of the unit cell would be attached when used in practice.

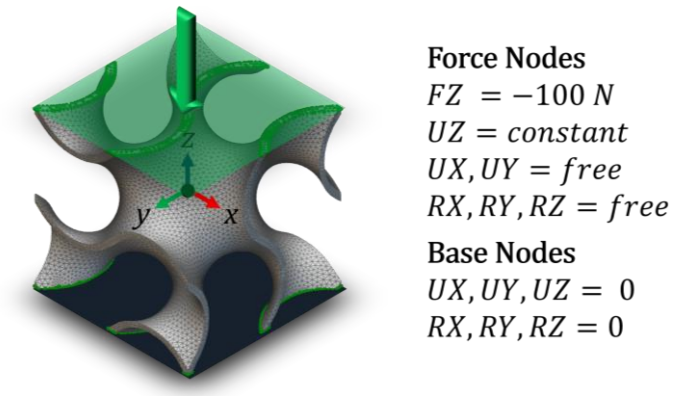

Figure 2.4. A gyroid sheet-TPMS scaffold with boundary conditions defined.

Geometry used in the study below is shown in Table 4.

Table 2. Sheet-TPMS geometries used.

Geometry type	**Gyroid (G)**	**Diamond (D)**	**Schwarz Primitive (P)**
Image	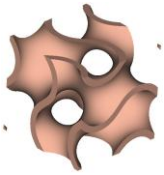	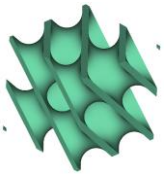	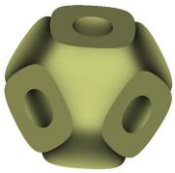

2.3 Simulation: Calculations

To ensure the desired stiffness was achieved consistently and effectively, an automated optimisation process was used. This removed the manual experimental process which would have required adapting the Gibson-Ashby model for each type of sheet-TPMS. It also allowed this methodology to be scaled across the three types of sheet-TPMS.

For each iteration, $i = 0, 1, 2, \ldots$ the current apparent stiffness, E_i, was calculated; and the absolute difference to the desired apparent stiffness, $E_{desired}$, was found. Apparent stiffness was defined as,

$$E_i = \frac{Fl}{A \cdot \Delta l} = \frac{F}{l \cdot \Delta l} \quad (1)$$

With variables defined as force, F; scaffold height, which in this case was the cell size, l; overall base area, $A = l^2$; and deformation in the z-axis for the current scaffold, Δl.

Should the percentage difference be greater than 5 percent difference, the next thickness, x_{new}, was then predicted using the secant root finding method. This was calculated iteratively with the equation,

$$(E_{desired} - E_i) = \frac{E_i - E_{i-1}}{x_i - x_{i-1}} \cdot (x_{new} - x_i) \text{ for } i = 0, 1, 2, \ldots \quad (2)$$

Where x_i corresponded to the thickness defined for the current scaffold.

2.4 Simulation: Mesh Convergence, Verification, and Validation

To ensure each iteration produced results that were converged, scaffolds with porosity between 50 to 90 percent were generated and simulated ahead of time to ensure the results with the specified mesh size converged. A mesh size of 0.05 mm was deemed appropriate after evaluating the results, which can be found in Appendix C.

Verification was then conducted by inspecting the results, the strain contours and deformation behaviours. Results were then modelled using the Gibson-Ashby model (Eq. 3), which has proven to hold excellent agreement for porous scaffolds with low relative density (or high porosity) [Gibson].

$$\frac{E_{scaffold}}{E_{material}} = C \left(\frac{\rho_{scaffold}}{\rho_{material}}\right)^n \quad (3)$$

Arbitrary coefficients C and n were obtained by fitting the curve to each set of data in MATLAB R2024b (Mathworks Inc, USA). This was also used to validate the optimised final design which was matched to a stiffness of 3 GPa.

Finally, to investigate the sensitivity of the stiffness under different configurations, the 2x2x2 cell configuration of the gyroid was used with the same boundary conditions.

3 RESULTS

3.1 Sheet-TPMS: Simulation Data

Illustrated below in Figure 3.1 are the converged results gathered from the initial simulations. The thickness of each sheet-TPMS was changed by increments of 0.1 mm from 0.1 to 0.5 mm. Cell size was kept constant at 3 mm.

Diamond (D) sheet-TPMS designs can be seen here as the stiffest, followed by gyroid (G) and primitive (P) at the same thicknesses. This observation is in line with the experimental data observed by Al-Ketan et al and Bobbert et al [17] [18].

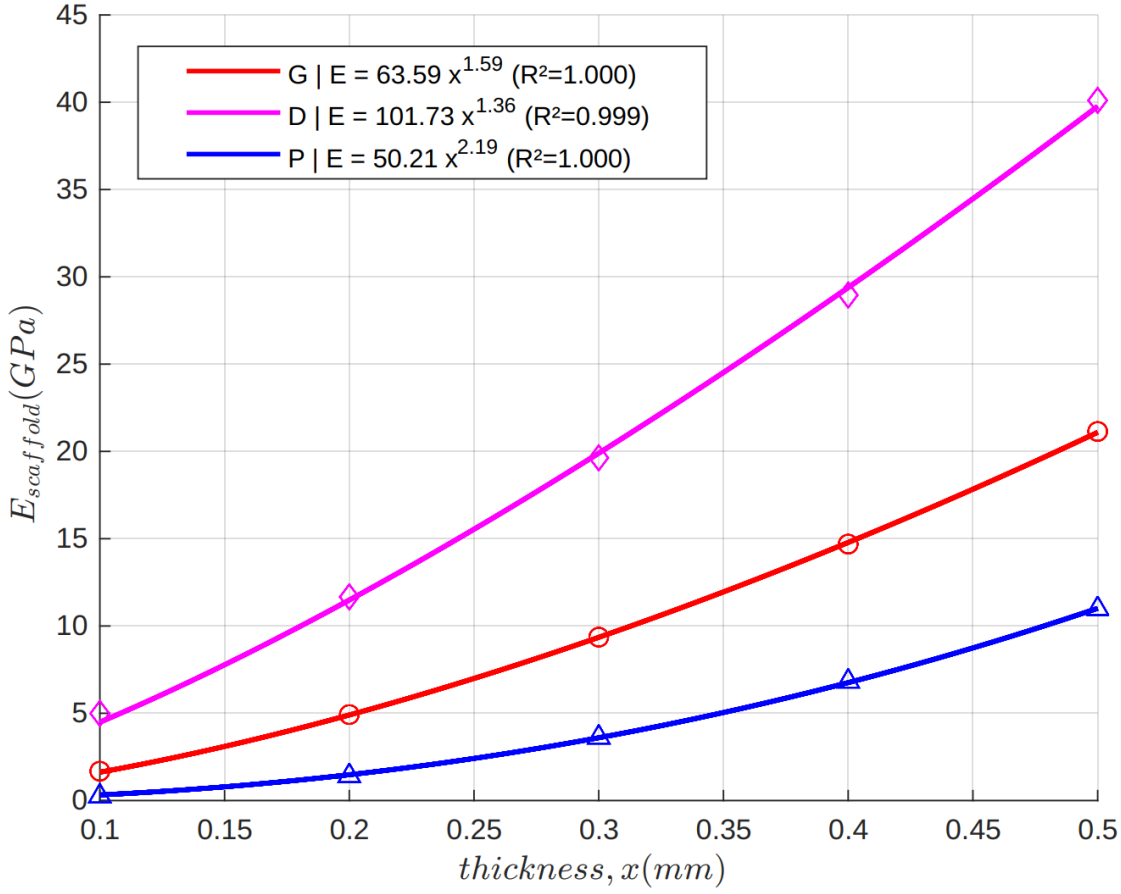

Figure 3.1. Apparent stiffness, $\boldsymbol{E_{scaffold}}$, against thickness, $\boldsymbol{x}$, from 0.1mm to 0.5 mm at a constant cell size of 3 mm.

3.2 *Sheet-TPMS: Gibson-Ashby Model*

By plotting the relative stiffness was calculated against the relative density, this allowed data to be compared with other data. As such, data from Simsek et al, who conducted a similar numerical study on sheet-TPMS scaffolds is included in Figure 3.4 [31].

Gyroid and diamond configurations here show excellent agreement with literature, albeit with a systematic error steadily which increased steadily. However, significant differences can be seen with the primitive (P) type, with the results showing an unusually high n value in the simulations conducted. This could be related to differences in cell configuration used, which affected the P type significantly. This is explored in Section 3.4.

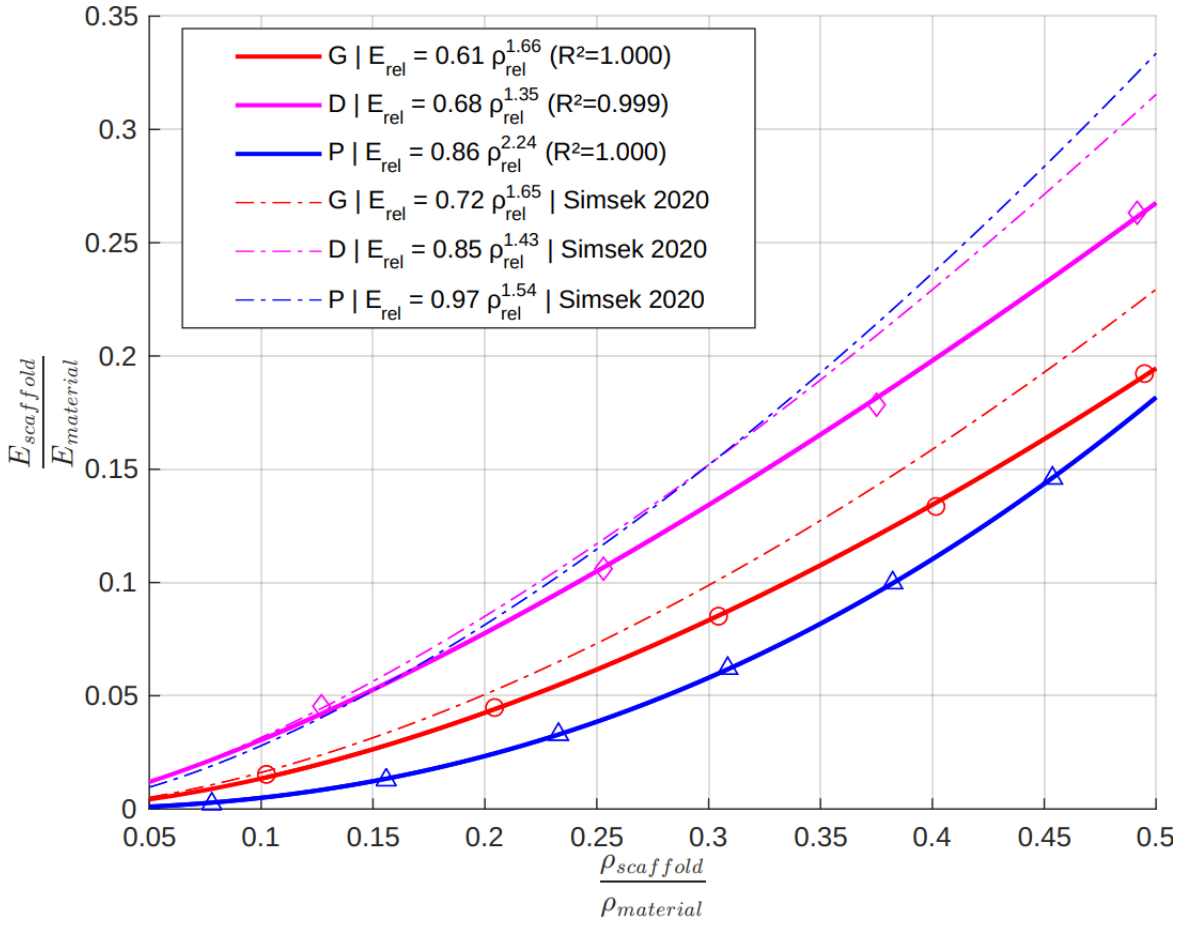

Figure 3.2. Relative stiffness, $\frac{E_{scaffold}}{E_{material}}$, against relative density, $\frac{\rho_{scaffold}}{\rho_{material}}$ from 0.05 to 0.5 (equivalent to porosity values from 95 down to 50 percent). Solid lines represent data modelled using the Gibson-Ashby model, whereas dotted lines represent data from Simsek et al **[31]**.

3.3 *Sheet-TPMS: Optimised Designs*

With the results modelled, each scaffold was then optimised to the desired apparent stiffness at 3.0 GPa, as shown in Figure 3.3.

All three scaffolds successfully achieved the desired tolerance within six iterations. The gyroid (G) converged with a percentage difference of 0.38%, whereas diamond (D) achieved 0.22%, and primitive (P) at 1.14%. Similar accuracy was obtained when the apparent stiffness was changed to other values.

The primitive configuration took longest to converge, as the initial values contributed to the low apparent stiffness, making it difficult to estimate the actual apparent stiffness.

Figure 3.4, Figure 3.5, and Figure 3.6 show the strain contours of each scaffold. Details of the results from this analysis is presented in Appendix D.

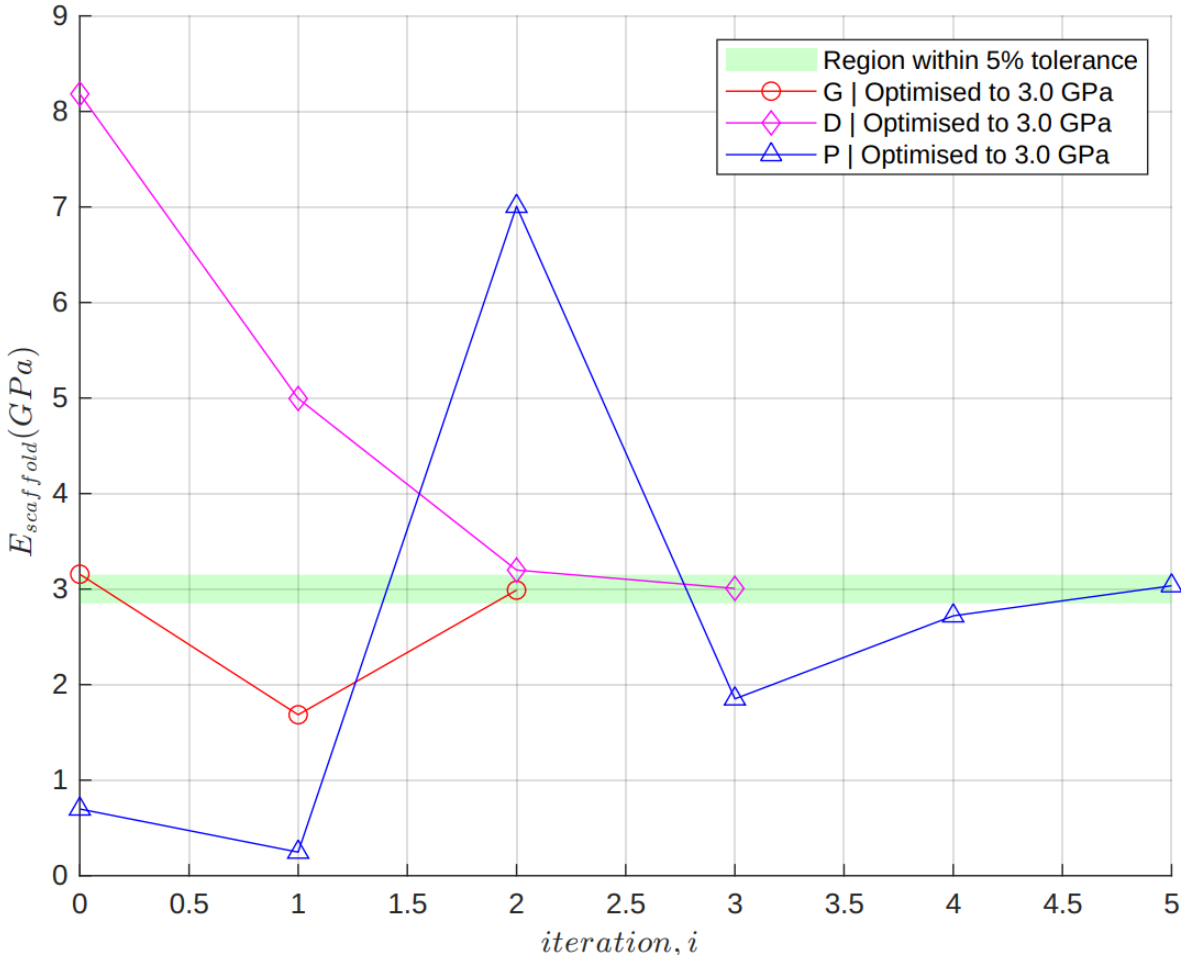

Figure 3.3. Apparent stiffness, $\boldsymbol{E_{scaffold}}$, of the scaffold over each iteration, $\boldsymbol{i}$. The apparent stiffness in this experiment was set to 3 GPa and a maximum tolerance of 5 percent was specified. This required the data to be between 2.85 GPa and 3.15 GPa, which was achieved by all three designs.

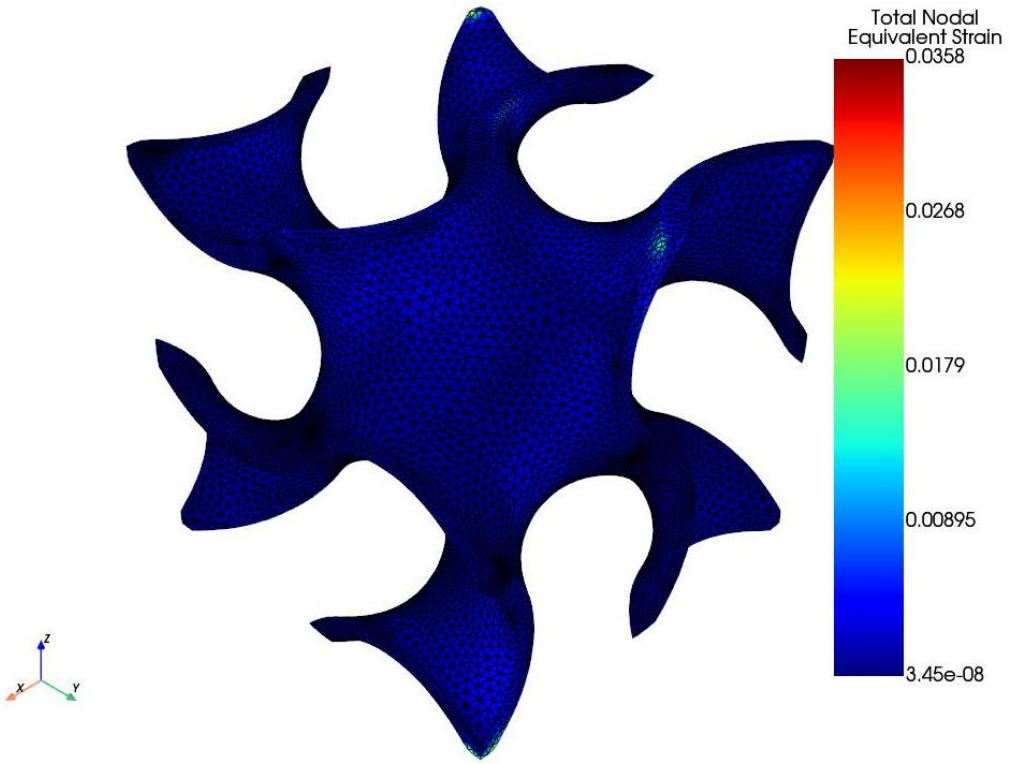

Figure 3.4. Optimised gyroid sheet-TPMS with thickness 0.1447 mm, porosity 85.2%, and apparent stiffness of 2.99 GPa. Minimal strain concentrations can be seen due to its smooth curvature.

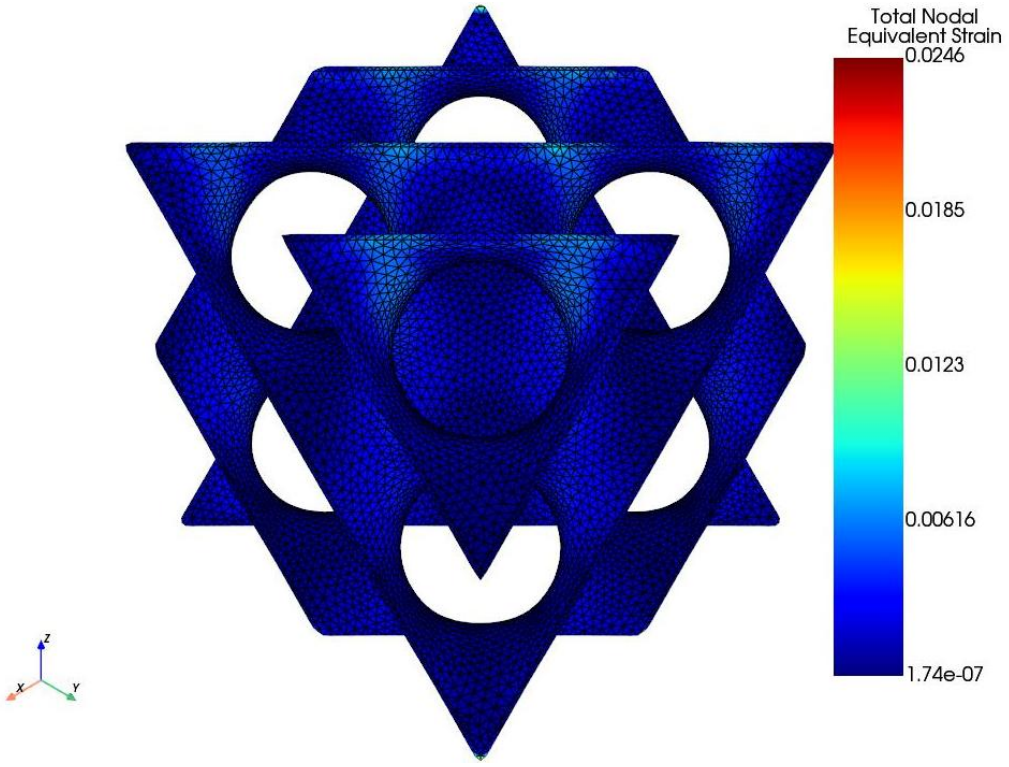

Figure 3.5. Optimised diamond sheet-TPMS with thickness 0.0653 mm, porosity 91.7% and apparent stiffness of 3.01 GPa. Minimal strain concentrations can be seen due to its smooth curvature.

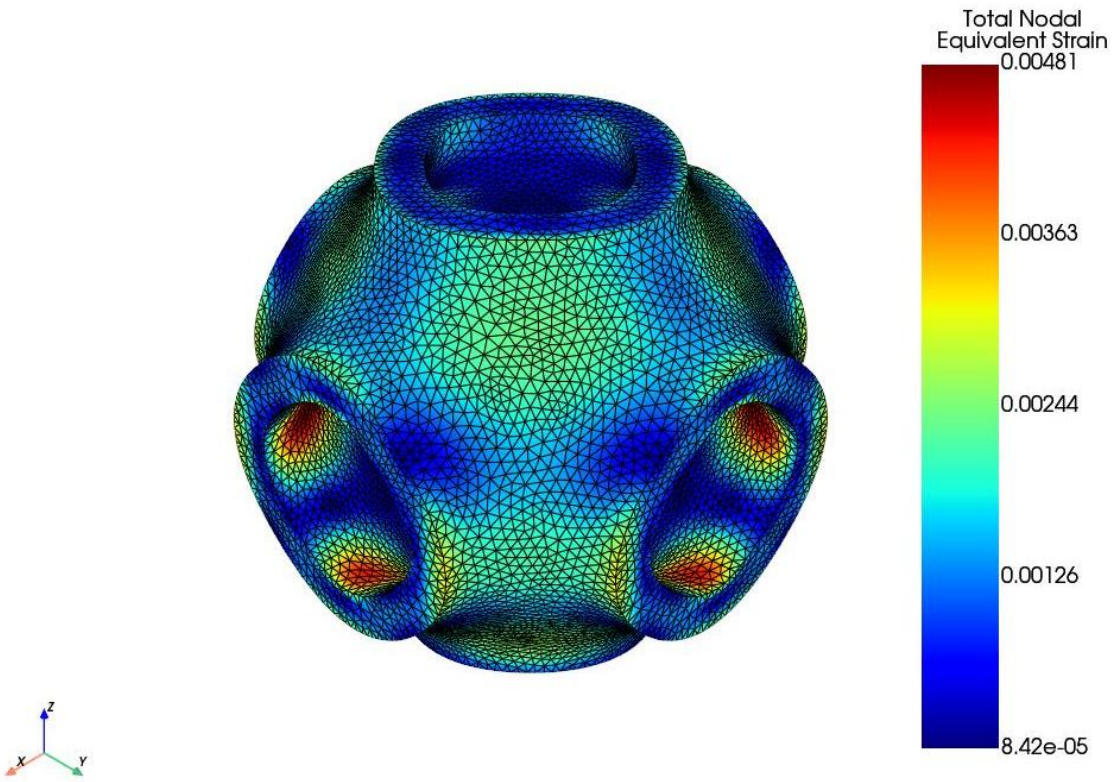

Figure 3.6. Optimised primitive sheet-TPMS with thickness 0.2775 mm, porosity 78.4% and apparent stiffness of 3.03 GPa. Larger regions of strain concentrations can be observed, likely contributing to the significantly lower apparent stiffness compared to gyroid and diamond.

3.4 Sheet-TPMS: Sensitivity Study

One interesting observation during this study was that sheet-TPMS scaffolds of the same thickness to cell size ratio, returned the same apparent stiffness and shared the same porosity. To investigate whether this would be the same when scaffolds are scaled up and multiplied in this framework, this was explored further in a sensitivity study.

This was achieved by simulating a 2x2x2 scaffold, as seen in Figure 3.7, and comparing it to an equivalent 1x1x1 configuration in Figure 3.1. Results showed that stiffness increased twofold.

This is in line with observations by Simsek et al, where the 1x1x1 configuration underestimated values significantly [31]. It highlights how in practice, strain patterns can be influenced by their surrounding geometry as well.

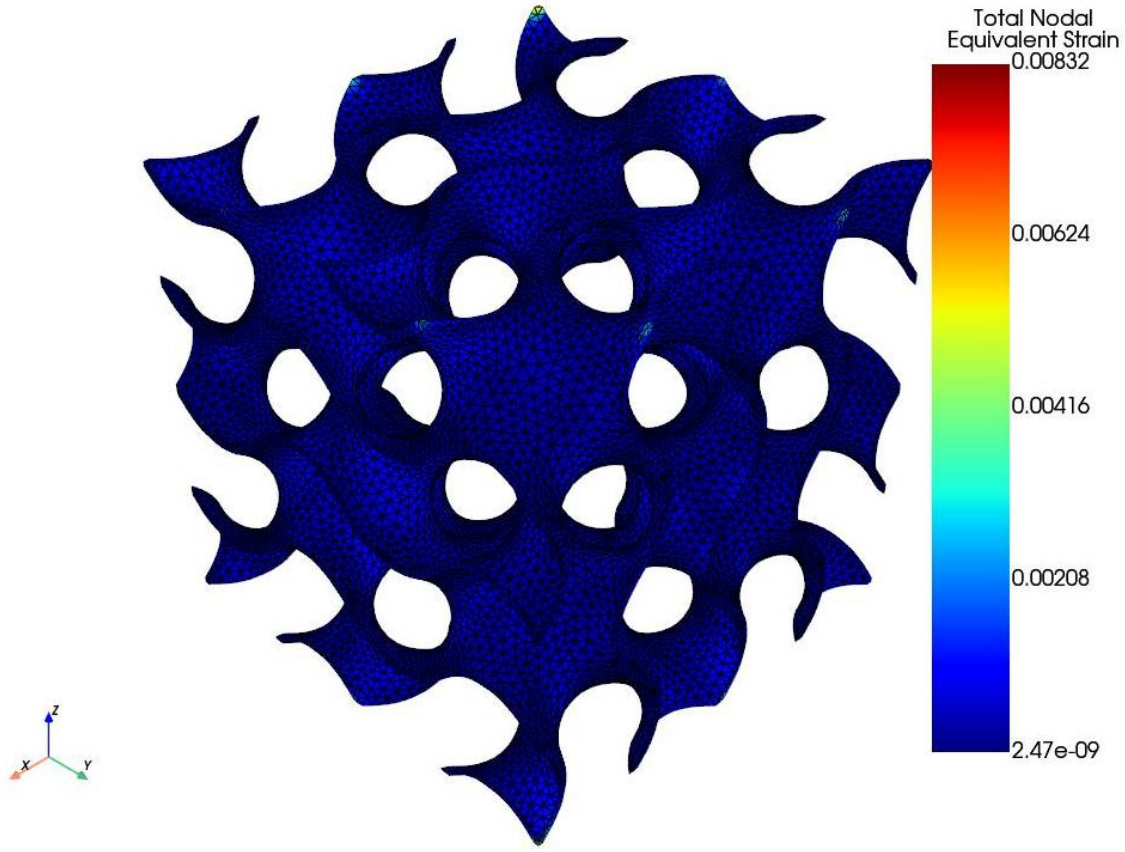

Figure 3.7. 2x2x2 gyroid sheet-TPMS scaffold with cell size 3 mm, thickness 0.1 mm, porosity 89.8%, and apparent stiffness of 3.21 GPa. This is almost two times larger than its 1x1x1 configuration.

4 DISCUSSION AND LIMITATIONS

In this study, the versatility of sheet-TPMS porous scaffolds and large stiffness range was shown and allowed the desired stiffness of 3.0 GPa to be achieved.

This was validated by using the analytical equations developed using the Gibson-Ashby model, as shown in Table 3. Interestingly, significant error was obtained for gyroid and diamond configurations. This could have been due to an error with the methodology used to calculate the relative density. On the other hand, due to the extremely low thickness, this would have been a contributing factor to the low accuracy when compared to the Gibson-Ashby model, as insufficient number of elements are available to capture the actual results in full detail.

Table 3. Optimised sheet-TPMS scaffolds compared to numerical results.

Type	Gibson-Ashby Equation	Relative Density	Analytical Relative Stiffness	Apparent Stiffness (GPa)	Numerical Relative Stiffness	Percentage Error
Gyroid	$0.61\ \rho_{rel}^{1.66}$	0.148	0.025583755	2.99	0.027181818	6.25%
Diamond	$0.68\ \rho_{rel}^{1.35}$	0.083	0.023619154	3.01	0.027363636	15.85%
Primitive	$0.86\ \rho_{rel}^{2.24}$	0.216	0.027776329	3.03	0.027545455	-0.83%

This study also highlights the fact that cell configuration needs to be considered when designing scaffolds to fit a certain apparent stiffness. While previous studies have suggested the importance of using a large cell configuration of 5x5x5 when analysed in numerically [Yang][Simsek], for the hip and knee implants where the porous surface is thin, this may be less important as the contributing factors from having larger number of unit cells in all directions would be negligible. This is an area for potential further research.

In practice, the low thickness (~0.1 mm) of sheet-TPMS scaffolds is difficult to manufacture, as a result it can be extremely inconsistent and problematic to control the apparent stiffness. There are solutions to this, and one way which has seen some popularity is by tweaking those parameters through experimentation. For instance, with selective laser sintering, changing the beam power, beam radius, hatching pattern, layer height, or scanning speed affects the metallic microstructure within the final product and therefore mechanical properties [38] [39] [40] [41].

As a result, integrating all these different properties into a single optimisation system is an area which could hold promise.

5 CONCLUSION

This study has investigated the use of numerical methods to achieve optimised porous scaffolds matched to a specific desired apparent stiffness efficiently. Gyroid, diamond and primitive sheet-TPMS scaffolds with a stiffness of 3.0 GPa were developed, with high accuracy to the desired stiffness.

Furthermore, a sensitivity study showed that cell configurations can hold significant impact, even though the porosity, cell size and thickness were kept constant. This was seen with the primitive design, where discrepancies were found when compared to another study.

An area for further research is to understand how sheet-TPMS scaffolds can be optimised in manufacturing. In addition, further development is necessary to consider partial bone ingrowth, where stress concentrations can be generated, and how significantly they can affect yield strength and fatigue strength when sheet-TPMS are used.

6 REFERENCES

[1] J. T. Evans, R. W. Walker, J. P. Evans, A. W. Blom, A. Sayers and M. R. Whitehouse, "How long does a knee replacement last? A systematic review and meta-analysis of case series and national registry reports with more than 15 years of follow-up," *The Lancet,* vol. 393, no. 10172, pp. 655-663, 2 2019.

[2] J. T. Evans, J. P. Evans, R. W. Walker, A. W. Blom, M. R. Whitehouse and A. Sayers, "How long does a hip replacement last? A systematic review and meta-analysis of case series and national registry reports with more than 15 years of follow-up," *The Lancet,* vol. 393, no. 10172, pp. 647-654, 2 2019.

[3] G. S. Matharu, D. J. Culliford, A. W. Blom and A. Judge, "Projections for primary hip and knee replacement surgery up to the year 2060: an analysis based on data from The National Joint Registry for England, Wales, Northern Ireland and the Isle of Man," *Annals of the Royal College of Surgeons of England,* vol. 104, no. 6, pp. 443-448, 6 2022.

[4] D. Culliford, J. Maskell, A. Judge, C. Cooper, D. Prieto-Alhambra and N. K. Arden, "Future projections of total hip and knee arthroplasty in the UK: results from the UK Clinical Practice Research Datalink," *Osteoarthritis and Cartilage,* vol. 23, no. 4, pp. 594-600, 4 2015.

[5] L. E. Bayliss, D. Culliford, A. P. Monk, S. Glyn-Jones, D. Prieto-Alhambra, A. Judge, C. Cooper, A. J. Carr, N. K. Arden, D. J. Beard and A. J. Price, "The effect of patient age at intervention on risk of implant revision after total replacement of the hip or knee: a population-based cohort study," *The Lancet,* vol. 389, no. 10077, pp. 1424-1430, 4 2017.

[6] M. Mercurio, G. Gasparini, V. Sanzo, F. Familiari, D. Castioni and O. Galasso, "Cemented Total Knee Arthroplasty Shows Less Blood Loss but a Higher Rate of Aseptic Loosening Compared With Cementless Fixation: An Updated Meta-Analysis of Comparative Studies," *The Journal of Arthoplasty,* vol. 37, no. 9, 2022.

[7] J. Moya-Angeler, M. Akkaya, M. Innocenti, D. Bergadano, J. Martin-Alguacil and V. León-Muñoz, "Fixation options for total knee arthroplasty: a comprehensive literature review," *Journal of Orthopaedic Surgery and Research,* vol. 19, no. 1, pp. 1-8, 12 2024.

[8] Y. Alshehri, P. D. Megaloikonomos, M. E. Neufeld, L. C. Howard, N. V. Greidanus, D. S. Garbuz and B. A. Masri, "Cementless Total Knee Arthroplasty: A State-of-The-Art Review," *JBJS Reviews,* vol. 12, no. 7, 7 2024.

[9] J. F. Baker, A. C. Nadar, A. C. Jouflas, L. S. Smith, S. Sachdeva, M. R. Yakkanti and A. L. Malkani, "Cementless metal-backed patellar components in primary total knee arthroplasty using an implant of modern design," *Bone Joint J,* vol. 105, no. 12, pp. 1279-1285, 2023.

[10] D. L. Bartel, D. T. Davy and T. M. Keaveny, Orthopaedic biomechanics : mechanics and design in musculoskeletal systems, D. T. Davy and T. M. Keaveny, Eds., Upper Saddle River, N.J.; London: Pearson/Prentice Hall, 2006.

[11] S. B. Goodman, Z. Yao, M. Keeney and F. Yang, "The future of biologic coatings for orthopaedic implants," *Biomaterials,* vol. 34, no. 13, pp. 3174-3183, 2013.

[12] E. Davoodi, H. Montazerian, A. S. Mirhakimi, M. Zhianmanesh, O. Ibhadode, S. I. Shahabad, R. Esmaeilizadeh, E. Sarikhani, S. Toorandaz, S. A. Sarabi, R. Nasiri, Y. Zhu, J. Kadkhodapour, B. Li, A. Khademhosseini and E. Toyserkani, "Additively manufactured metallic biomaterials," *Bioactive Materials,* vol. 15, pp. 214-249, 9 2022.

[13] G. L. Rasmussen, "Lessons Learned from Cementless Fixation," *Total Knee Arthroplasty: A Guide to Get Better Performance,* pp. 101-106, 2005.

[14] R. Hedayati, S. Janbaz, M. Sadighi, M. Mohammadi-Aghdam and A. Zadpoor, "How does tissue regeneration influence the mechanical behavior of additively manufactured porous biomaterials?," *Journal of the Mechanical Behavior of Biomedical Materials,* vol. 65, pp. 831-841, 1 2017.

[15] A. A. Zadpoor, "Bone tissue regeneration: the role of scaffold geometry," *Biomaterials Science,* vol. 3, no. 2, pp. 231-245, 1 2015.

[16] S. Ghouse, N. Reznikov, O. R. Boughton, S. Babu, K. G. Ng, G. Blunn, J. P. Cobb, M. M. Stevens and J. R. Jeffers, "The design and in vivo testing of a locally stiffness-matched porous scaffold," *Applied Materials Today,* vol. 15, pp. 377-388, 6 2019.

[17] O. Al-Ketan, R. Rowshan and R. K. Abu Al-Rub, "Topology-mechanical property relationship of 3D printed strut, skeletal, and sheet based periodic metallic cellular materials," *Additive Manufacturing,* vol. 19, pp. 167-183, 1 2018.

[18] F. Bobbert, K. Lietaert, A. Eftekhari, B. Pouran, S. Ahmadi, H. Weinans and A. Zadpoor, "Additively manufactured metallic porous biomaterials based on

minimal surfaces: A unique combination of topological, mechanical, and mass transport properties," *Acta Biomaterialia,* vol. 53, pp. 572-584, 4 2017.

[19] C. Perier-Metz, G. N. Duda and S. Checa, "Initial mechanical conditions within an optimized bone scaffold do not ensure bone regeneration – an in silico analysis," *Biomechanics and Modeling in Mechanobiology,* vol. 20, no. 5, pp. 1723-1731, 10 2021.

[20] E. Maevskaia, J. Guerrero, C. Ghayor, I. Bhattacharya and F. E. Weber, "Triply Periodic Minimal Surface-Based Scaffolds for Bone Tissue Engineering: A Mechanical, In Vitro and In Vivo Study," *Tissue Engineering - Part A,* vol. 29, no. 19-20, pp. 507-517, 10 2023.

[21] N. Taniguchi, S. Fujibayashi, M. Takemoto, K. Sasaki, B. Otsuki, T. Nakamura, T. Matsushita, T. Kokubo and S. Matsuda, "Effect of pore size on bone ingrowth into porous titanium implants fabricated by additive manufacturing: An in vivo experiment," *Materials Science and Engineering: C,* vol. 59, pp. 690-701, 2 2016.

[22] V. S. Cheong, P. Fromme, M. J. Coathup, A. Mumith and G. W. Blunn, "Partial Bone Formation in Additive Manufactured Porous Implants Reduces Predicted Stress and Danger of Fatigue Failure," *Annals of Biomedical Engineering,* vol. 48, no. 1, pp. 502-514, 1 2020.

[23] V. Karageorgiou and D. Kaplan, "Porosity of 3D biomaterial scaffolds and osteogenesis," *Biomaterials,* vol. 26, no. 27, pp. 5474-5491, 9 2005.

[24] K. Kapat, P. K. Srivas, A. P. Rameshbabu, P. P. Maity, S. Jana, J. Dutta, P. Majumdar, D. Chakrabarti and S. Dhara, "Influence of Porosity and Pore-Size Distribution in Ti6Al4 v Foam on Physicomechanical Properties, Osteogenesis, and Quantitative Validation of Bone Ingrowth by Micro-Computed Tomography," *ACS Applied Materials and Interfaces,* vol. 9, no. 45, pp. 39235-39248, 11 2017.

[25] J. Van Der Stok, O. P. Van Der Jagt, S. Amin Yavari, M. F. De Haas, J. H. Waarsing, H. Jahr, E. M. Van Lieshout, P. Patka, J. A. Verhaar, A. A. Zadpoor and H. Weinans, "Selective laser melting-produced porous titanium scaffolds regenerate bone in critical size cortical bone defects," *Journal of Orthopaedic Research,* vol. 31, no. 5, pp. 792-799, 5 2013.

[26] S. H. Wu, Y. Li, Y. Q. Zhang, X. K. Li, C. F. Yuan, Y. L. Hao, Z. Y. Zhang and Z. Guo, "Porous Titanium-6 Aluminum-4 Vanadium Cage Has Better Osseointegration and Less Micromotion Than a Poly-Ether-Ether-Ketone Cage in Sheep Vertebral Fusion," *Artificial Organs,* vol. 37, no. 12, pp. E191-E201, 12 2013.

[27] D. Apostu, O. Lucaciu, C. Berce, D. Lucaciu and D. Cosma, “Current methods of preventing aseptic loosening and improving osseointegration of titanium implants in cementless total hip arthroplasty: a review,” *Journal of International Medical Research,* vol. 46, no. 6, pp. 2104-2119, 6 2018.

[28] V. S. Cheong, P. Fromme, A. Mumith, M. J. Coathup and G. W. Blunn, “Novel adaptive finite element algorithms to predict bone ingrowth in additive manufactured porous implants,” *Journal of the Mechanical Behavior of Biomedical Materials,* vol. 87, pp. 230-239, 11 2018.

[29] M. Ding, M. Dalstra, C. C. Danielsen, J. Kabel, I. Hvid and F. Linde, “AGE VARIATIONS IN THE PROPERTIES OF HUMAN TIBIAL TRABECULAR BONE,” *The Journal of Bone & Joint Surgery British Volume,* Vols. 79-B, no. 6, pp. 995-1002, 11 1997.

[30] S. Ghouse, S. Babu, K. Nai, P. A. Hooper and J. R. Jeffers, “The influence of laser parameters, scanning strategies and material on the fatigue strength of a stochastic porous structure,” *Additive Manufacturing,* vol. 22, pp. 290-301, 8 2018.

[31] U. Simsek, A. Akbulut, C. E. Gayir, C. Basaran and P. Sendur, “Modal characterization of additively manufactured TPMS structures: comparison between different modeling methods,” *International Journal of Advanced Manufacturing Technology,* vol. 115, no. 3, pp. 657-674, 7 2021.

[32] N. Sabahi, E. Farajzadeh, I. Roohani, C. H. Wang and X. Li, “Material extrusion 3D printing of polyether-ether-ketone scaffolds based on triply periodic minimal surface designs: A numerical and experimental investigation,” *Applied Materials Today,* vol. 39, p. 102262, 8 2024.

[33] V. Baumer, E. Gunn, V. Riegle, C. Bailey, C. Shonkwiler and D. Prawel, “Robocasting of Ceramic Fischer–Koch S Scaffolds for Bone Tissue Engineering,” *Journal of Functional Biomaterials 2023, Vol. 14, Page 251,* vol. 14, no. 5, p. 251, 4 2023.

[34] P. A. Khan, A. Raheem, C. Kalirajan, K. G. Prashanth and G. Manivasagam, “In Vivo Assessment of a Triple Periodic Minimal Surface Based Biomimmetic Gyroid as an Implant Material in a Rabbit Tibia Model,” *ACS Materials Au,* vol. 4, no. 5, pp. 479-488, 9 2024.

[35] C. H. P. Nguyen, Y. Kim, Q. T. Do and Y. Choi, “Implicit-based computer-aided design for additively manufactured functionally graded cellular structures,”

Journal of Computational Design and Engineering, vol. 8, no. 3, pp. 813-823, 5 2021.

[36] G. Allen, "nTop Implicit Modeling Technology Whitepaper," [Online]. Available: https://49037331.fs1.hubspotusercontent-na1.net/hubfs/49037331/eBooks%20and%20Guides%20-%20Approved%20Assets/Whitepaper-Implicit_modeling_technology-4.pdf?utm_medium=email&_hsenc=p2ANqtz--_oul_ANgaUVU3lOsDX1_mZI8pGtIR367wCLoQGYNKZep2f9rl-yJd_GT5r19lIMl45Sv-2bet_IcDMWTQ5PIjEjX4QA&_hsmi=351986037&utm_content=351986037&utm_source=hs_automation. [Accessed 28 4 2025].

[37] Hong Daeho, "From implicit to print without making a mesh | nTop," 10 10 2022. [Online]. Available: https://www.ntop.com/resources/product-updates/from-implicit-to-print/.

[38] S. Ghouse, S. Babu, R. J. Van Arkel, K. Nai, P. A. Hooper and J. R. Jeffers, "The influence of laser parameters and scanning strategies on the mechanical properties of a stochastic porous material," *Materials & Design,* vol. 131, pp. 498-508, 10 2017.

[39] Z. Wang, Z. Xiao, Y. Tse, C. Huang and W. Zhang, "Optimization of processing parameters and establishment of a relationship between microstructure and mechanical properties of SLM titanium alloy," *Optics & Laser Technology,* vol. 112, pp. 159-167, 4 2019.

[40] F. S. Freeman, L. M. Jones, A. D. Goodall, H. Ghadbeigi and I. Todd, "Structural metamaterial lattices by laser powder-bed fusion of 17-4PH steel," *Additive Manufacturing Letters,* vol. 8, p. 100190, 2 2024.

[41] D. Mahmoud, K. S. Al-Rubaie and M. A. Elbestawi, "The influence of selective laser melting defects on the fatigue properties of Ti6Al4V porosity graded gyroids for bone implants," *International Journal of Mechanical Sciences,* vol. 193, p. 106180, 3 2021.

[42] S. Sturm, S. Zhou, Y. W. Mai and Q. Li, "On stiffness of scaffolds for bone tissue engineering—a numerical study," *Journal of Biomechanics,* vol. 43, no. 9, pp. 1738-1744, 6 2010.

[43] N. Qiu, Y. Wan, Y. Shen and J. Fang, "Experimental and numerical studies on mechanical properties of TPMS structures," *International Journal of Mechanical Sciences,* vol. 261, p. 108657, 1 2024.

[44] V. S. Deshpande, M. F. Ashby and N. A. Fleck, “Foam topology: bending versus stretching dominated architectures,” *Acta Materialia,* vol. 49, no. 6, pp. 1035-1040, 4 2001.

[45] National Institute for Health and Care Excellence, “Impact on NHS workforce and resources | Joint replacement (primary): hip, knee and shoulder | Guidance | NICE,” 6 2020.

[46] L. J. Gibson, “The mechanical behaviour of cancellous bone,” *Journal of Biomechanics,* vol. 18, no. 5, pp. 317-328, 1 1985.

[47] I. D. Learmonth, C. Young and C. Rorabeck, “The operation of the century: total hip replacement,” *Lancet,* vol. 370, no. 9597, pp. 1508-1519, 10 2007.

APPENDICES

Appendix A

Code is available upon request.

Appendix B

Table 4. Sheet-TPMS design specifications. Figures adapted from nTop Support.

Geometry type	Gyroid (G)	Diamond (D)	Schwarz Primitive (P)
Image	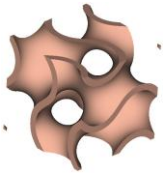	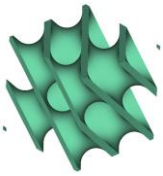	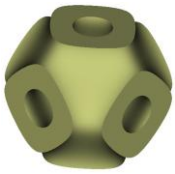
Equation	$\sin(x)\sin(y) + \sin(y)\sin(z) + \sin(z)\cos(y)$	$\sin(x)\sin(y)\sin(z) + \sin(x)\cos(y)\cos(z) + \cos(x)\sin(y)\cos(z) + \cos(x)\cos(y)\sin(z)$	$\cos(x) + \cos(y) + \cos(z)$

Appendix C

Table 5. Mesh convergence analysis for Gyroid Sheet-TPMS

Execution Time (s)	Element Num	Thickness (mm)	Porosity	Element Size (mm)	Internal Stress (Pa)	Strain	Apparent Stiffness (Pa)	% Change
100	12067	0.1	89.80%	0.1	5.04E+09	0.006578	1.69E+09	
191	120022	0.1	89.77%	0.05	5.25E+09	0.006598	1.68E+09	-0.31%
544	471118	0.1	89.74%	0.033	6.42E+09	0.006580	1.69E+09	0.27%
75	3429	0.2	79.28%	0.2	8.93E+08	0.002157	5.15E+09	
89	30417	0.2	79.62%	0.1	1.26E+09	0.002240	4.96E+09	-3.73%
381	294395	0.2	79.57%	0.05	2.67E+09	0.002255	4.93E+09	-0.64%
71	6393	0.3	69.13%	0.2	4.40E+08	0.001141	9.74E+09	
98	52303	0.3	69.59%	0.1	7.78E+08	0.001179	9.43E+09	-3.18%
716	453983	0.3	69.56%	0.05	1.18E+09	0.001187	9.36E+09	-0.66%
4124	1579246	0.3	69.54%	0.033	1.41E+09	0.001189	9.35E+09	-0.19%
66	8463	0.4	59.29%	0.2	3.03E+08	0.000728	1.53E+10	
112	73041	0.4	59.82%	0.1	4.63E+08	0.000751	1.48E+10	-3.01%
1123	622206	0.4	59.84%	0.05	8.45E+08	0.000756	1.47E+10	-0.73%
55	11702	0.5	49.83%	0.2	2.33E+08	0.000506	2.20E+10	
133	96903	0.5	50.49%	0.1	3.26E+08	0.000521	2.13E+10	-3.02%
1715	771170	0.5	50.52%	0.05	7.72E+08	0.000526	2.11E+10	-0.80%

Table 6. Mesh convergence analysis for Diamond Sheet-TPMS

Execution Time (s)	Element Num	Thickness (mm)	Porosity	Element Size (mm)	Internal Stress (Pa)	Strain	Apparent Stiffness (Pa)	% Change
88	14873	0.1	87.36%	0.1	9.03E+08	0.002220	5.00E+09	
222	151403	0.1	87.31%	0.05	9.88E+08	0.002225	4.99E+09	-0.20%
685	574947	0.1	87.26%	0.033	9.39E+08	0.002227	4.99E+09	-0.09%
62	5699	0.2	74.11%	0.2	2.01E+08	0.000906	1.23E+10	
90	38666	0.2	74.74%	0.1	2.45E+08	0.000944	1.18E+10	-3.98%
470	370151	0.2	74.70%	0.05	4.57E+08	0.000952	1.17E+10	-0.86%
2433	1263796	0.2	74.68%	0.033	4.45E+08	0.000954	1.16E+10	-0.20%
65	11761	0.3	62.05%	0.2	1.16E+08	0.000545	2.04E+10	
120	63017	0.3	62.39%	0.1	1.30E+08	0.000559	1.99E+10	-2.49%
885	556005	0.3	62.49%	0.05	1.84E+08	0.000566	1.96E+10	-1.24%
78	19413	0.4	50.19%	0.2	1.28E+08	0.000371	3.00E+10	
132	87170	0.4	50.73%	0.1	9.50E+07	0.000379	2.93E+10	-2.20%
1580	759266	0.4	50.85%	0.05	1.82E+08	0.000384	2.90E+10	-1.16%
73	35146	0.5	39.56%	0.25	8.81E+07	0.000272	4.09E+10	
160	123698	0.5	39.83%	0.1	1.26E+08	0.000277	4.01E+10	-1.96%
N/A*	N/A*	0.5	N/A*	0.05	N/A*	N/A*	N/A*	N/A*

* = Unavailable due to exceeding maximum RAM or runtime allocated

Table 7. Mesh convergence analysis for Primitive Sheet-TPMS

Execution Time (s)	Element Num	Thickness (mm)	Porosity	Element Size (mm)	Internal Stress (Pa)	Strain	Apparent Stiffness (Pa)	% Change
100	9349	0.1	92.23%	0.1	2.86E+09	0.044595	2.49E+08	
163	92578	0.1	92.21%	0.05	2.78E+09	0.045162	2.46E+08	-1.26%
67	2919	0.2	84.14%	0.2	7.60E+08	0.007330	1.52E+09	
86	22352	0.2	84.47%	0.1	8.62E+08	0.007842	1.42E+09	-6.53%
257	218955	0.2	84.41%	0.05	8.96E+08	0.007879	1.41E+09	-0.47%
63	4079	0.3	76.60%	0.2	4.13E+08	0.002942	3.78E+09	
97	38654	0.3	76.74%	0.1	4.46E+08	0.003053	3.64E+09	-3.63%
437	346345	0.3	76.71%	0.05	4.64E+08	0.003069	3.62E+09	-0.51%
67	6551	0.4	68.85%	0.2	2.56E+08	0.001549	7.17E+09	
113	53834	0.4	69.17%	0.1	2.81E+08	0.001618	6.87E+09	-4.31%
738	469188	0.4	69.15%	0.05	3.00E+08	0.001628	6.83E+09	-0.58%
69	8799	0.5	61.46%	0.2	1.95E+08	0.000982	1.13E+10	
124	68843	0.5	61.76%	0.1	2.09E+08	0.001004	1.11E+10	-2.22%
1131	587337	0.5	61.77%	0.05	2.17E+08	0.001012	1.10E+10	-0.78%

Appendix D

Table 8. Sheet-TPMS scaffolds optimised to 3.0 GPa with a maximum tolerance of 5 percent.

Type	Execution Time (s)	Element Num	Node Num	Thickness (s)	Porosity	Internal Stress (Pa)	Strain	Apparent Stiffness (Pa)	% Difference
Gyroid	286	219904	332188	0.1500	84.6%	3.01E+09	0.00352	3.16E+09	5.17%
	199	120022	193593	0.1000	89.8%	5.25E+09	0.00660	1.68E+09	-43.87%
	270	198769	299240	0.1447	85.2%	3.55E+09	0.00372	2.99E+09	-0.38%
Diamond	349	257925	386299	0.1500	81.0%	4.59E+08	0.00136	8.18E+09	172.77%
	249	151403	245229	0.1000	87.3%	9.88E+08	0.00222	4.99E+09	66.47%
	170	65224	126502	0.0687	91.3%	2.45E+09	0.00347	3.2E+09	6.63%
	174	65655	129579	0.0653	91.7%	2.71E+09	0.00370	3.01E+09	0.22%
Primitive	207	155669	231972	0.1500	88.3%	1.43E+09	0.01592	6.98E+08	-76.74%
	152	92578	149005	0.1000	92.2%	2.78E+09	0.04516	2.46E+08	-91.80%
	769	470732	651200	0.4050	68.8%	2.97E+08	0.00159	7.01E+09	133.55%
	311	251059	358890	0.2242	82.5%	7.34E+08	0.00600	1.85E+09	-38.31%
	384	300681	425299	0.2645	79.4%	5.64E+08	0.00409	2.72E+09	-9.34%
	428	317526	447866	0.2775	78.4%	5.29E+08	0.00366	3.03E+09	1.14%